PhotoniX

Nonvolatile reconfigurable terahertz wave modulator

Shoujun Zhang[1], Xieyu Chen[1], Kuan Liu[2], Haiyang Li[2], Yuehong Xu[1], Xiaohan Jiang[1], Yihan Xu[1], Qingwei Wang[1], Tun Cao[2]* and Zhen Tian[1,3]*

*Correspondence:
caotun1806@dlut.edu.cn;
tianzhen@tju.edu.cn
[2] School of Optoelectronic
Engineering
and Instrumentation
Science, Dalian University
of Technology, Dalian 116024,
People's Republic of China
[3] Georgia Tech Shenzhen
Institute (GTSI), Tianjin
University, Shenzhen 518067,
China
Full list of author information
is available at the end of the
article

Abstract

Miniaturized nonvolatile reconfigurable optical components with a subwavelength thickness, extremely compact size, high-speed response, and low power consumption will be the core of next-generation all-optical integrated devices and photonic computing to replace traditional bulky optical devices and integrated circuits, which are reaching physical limitations of Moore's law. Metasurfaces, as ultrathin planar surfaces, have played a major role in controlling the amplitude, phase, and polarization of electromagnetic waves and can be combined with various active modulation methods to realize a variety of functional devices. However, most existing reconfigurable devices are bounded in volatile nature with constant power to maintain and single functionality, which restricts their further extensive applications. Chalcogenide phase change materials (PCM) have attracted considerable attention due to their unique optical properties in the visible and infrared domains, whereas in the terahertz (THz) regime, research on the reversible phase transition in large-scale areas and applications of $Ge_2Sb_2Te_5$ (GST) are still under exploration. Here, we achieved reversible, repeated, and large-area switching of GST with the help of optical and thermal stimuli. Large-area amorphization with a 1 cm diameter of GST is realized by using a single laser pulse. Then, we incorporate GST into metasurface designs to realize nonvolatile, reconfigurable, multilevel, and broadband terahertz modulators, including the anomalous deflector, metalens, and focusing optical vortex (FOV) generator. Experimental results verify the feasibility of multilevel modulation of THz waves in a broadband frequency range. Moreover, the modulators are reusable and nonvolatile. The proposed approach presents novel avenues of nonvolatile and reconfigurable metasurface designs and can enable wide potential applications in imaging, sensing, and high-speed communications.

Keywords: Nonvolatile, Reconfigurable, Modulator, Phase change material, Terahertz

Introduction

The terahertz radiation, covering the frequency range from 0.1 to 10 THz, is located between the microwave and infrared regions due to its extraordinary properties, including nonionizing without damage to biological tissues, better penetration than optical bands, unique spectral fingerprints, and higher available bandwidth [1–5], and has tremendous application potential in the fields of spectroscopy [6, 7], sensing [8, 9], imaging

[10], security inspection [11], and high-speed communication [12, 13]. The development of miniaturized and integrated devices that control the wavefront, phase, and polarization of terahertz waves is essential to enable these applications [14–16]. However, the existing THz modulation devices have few types and are bulky and cannot meet the increasing demand.

The metasurface is an ultrathin planar surface composed of subwavelength artificial microstructures. It is a two-dimensional version of a metamaterial, which overcomes many shortcomings of metamaterials, including complicated design and large volume. Metasurfaces deliver an exceptional ability in controlling the phase [17–19], amplitude [20], and polarization [21, 22] and realizing a complex field distribution [23–25] in the transmission/reflection of electromagnetic waves. The thickness commensurate with the subwavelength makes the metasurfaces very suitable for the development of integrated devices [26, 27]. Recently, a variety of terahertz ultrathin modulation devices have been realized by using metasurfaces, including flat lenses [28, 29], anomalous refraction/reflection [19, 30, 31], vortex generators [17, 32], holographic imaging [33], and efficient surface plasmon couplers [34, 35].

Although metasurfaces play a great role in manipulating electromagnetic waves, their properties are static and cannot be changed after fabrication, which functions as passive devices with a single functionality and restricts their further extensive applications. Therefore, it is essential to develop tunable and reconfigurable devices that can actively control electromagnetic waves. In recent years, various methods have been proposed to realize tunable terahertz metasurfaces, including liquid crystals (LCs) [36, 37], semiconductors [38, 39], MEMS [40–43], graphene [44, 45] and phase change materials [20, 46–49], whose optical properties can be tuned via thermal [20, 46], optical [39, 47–49], or electrical stimuli [36–38, 44, 45]. These active modulation methods have demonstrated extraordinary capabilities in the realization of various functional devices [20, 36–50] such as terahertz spatial light modulators, waveplates, holography, and electromagnetically induced transparency. However, most of the methods mentioned above have a volatile response that requires a constant stimulus to maintain and a complicated fabrication process over a large area.

The chalcogenide phase change material (PCM) $Ge_2Sb_2Te_5$ (GST) has attracted increasing attention due to its unique phase-change characteristics [47–49, 51–59]. Structural transformation can be achieved through thermal, electrical, and optical stimuli, enabling nonvolatile random storage memory devices. Compared with other active media, the reversible transition between the amorphous state and the crystalline state of GST is nonvolatile and does not require constant energy to maintain. In addition, GST exhibits a dramatic difference in optical properties between amorphous and crystalline states, and there are many intermediate states, i.e., part crystalline and part amorphous, which can be switched quickly (nanosecond) and repeatedly (up to 10^{15} cycles) [57] between these states. Moreover, these states are stable for years at room temperature [59]. Given these excellent properties, GST has been used in the development of integrated all-optical memory devices [53, 54], photonic neuromorphic devices [55, 56], color displays [57], and plasmonic and dielectric metasurfaces [58].
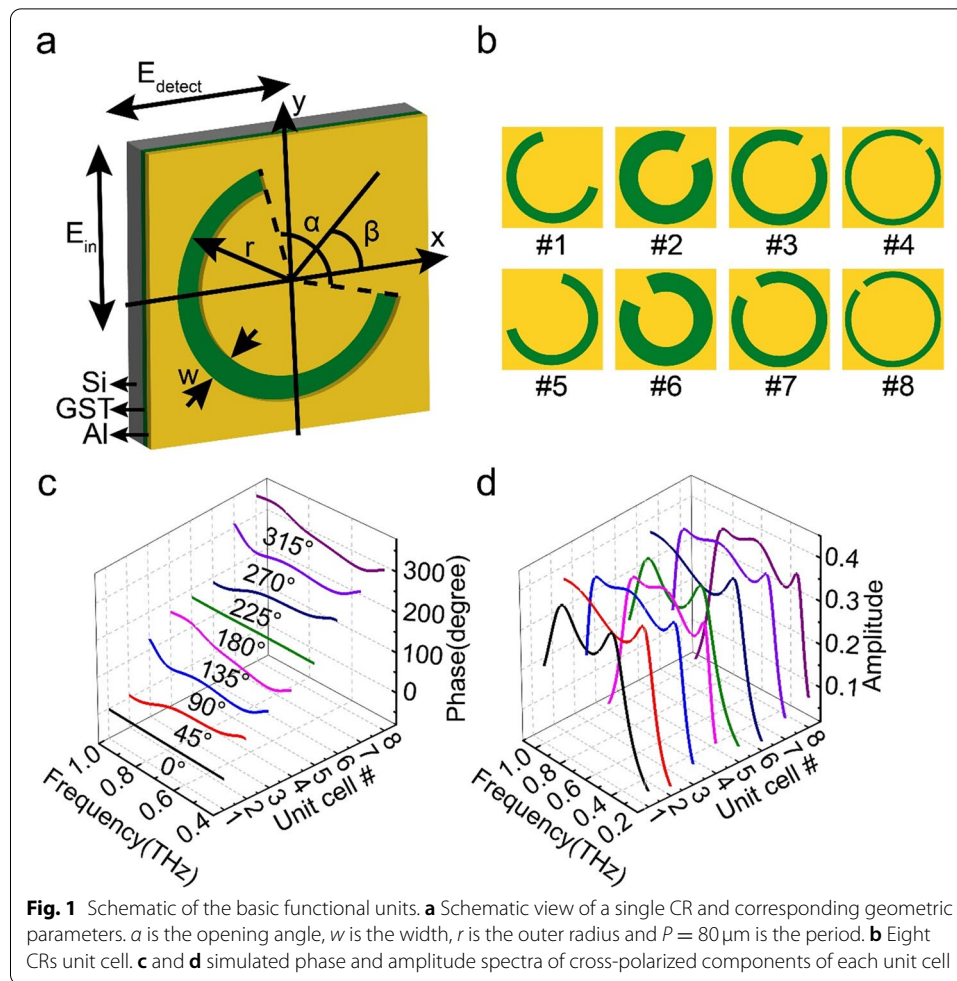
However, in the terahertz band, there are few studies on the reversible phase transition of GST on large-scale areas and studies on the realization of terahertz reconfigurable,

nonvolatile, and functional devices by controlling the phase, amplitude, and wavefront of terahertz waves, which is crucial for enabling a wider range of terahertz applications [47−49]. We note that a coding metasurface with reconfiguration capabilities based on GeTe has been proposed in the terahertz band. In this work, the device needed mask alignment to achieve encoding and worked in reflection mode, which is limited to complex processing procedures and working modes [59].

In this work, we combine the phase change material GST and phase-discontinuities metasurfaces to realize nonvolatile, reconfigurable, multilevel, and broadband terahertz functional devices, including anomalous deflectors, metalenses, and focusing optical vortex generators. In the terahertz band, GST exhibits dramatic differences in conductivity between amorphous (2000 S/m) and crystalline (2×10^5 S/m) states, which exhibit high and low transmittance, respectively (Supporting information, Fig. S1). Here, by adopting C-shaped slit resonators (CRs) with phase discontinuities, we propose terahertz wavefront-shaped modulation devices. We design and fabricate samples and experimentally examine the characteristics of modulation devices by a fiber-based angle-resolved terahertz time-domain spectroscopy (FAT-TDS) system and a near-field scanning terahertz microscopy (NSTM) system. We induce crystallization by heating the entire device on a hot plate at 300 °C for 2 min and reamorphization by a single 7-ns laser pulse with 120 mJ/cm² to realize repeated switching. In addition, by tuning the laser influence, intermediate states are realized, which are applied for multilevel modulation. Compared with the existing tunable approaches, our proposed THz modulators exhibit following several distinctive advantages: (i) The devices are nonvolatile and energy-efficient. By applying optical or thermal stimulus, amorphous, crystalline or intermediate states are formed, which are stable in a certain phase state for years at room temperature after removing the external energy. (ii) There is dramatic contrast in conductivity at both states (amorphous and crystalline) of GST, which results in a large difference in THz transmission. In the amorphous state, the THz functional devices are effective, and in the crystalline state, the devices are turned off. By switching between both states, we can realize 'ON' and 'OFF' states. (iii) There are many intermediate states between amorphous and crystalline states, which can be exploited to enable multilevel modulators. (iv) The devices exhibit broadband feature from 0.4 THz to 0.8 THz. The proposed functional metasurfaces combined with GST pave a novel way to realize reconfigurable and nonvolatile terahertz devices and might have essential applications in terahertz integrated devices, imaging, and communications.
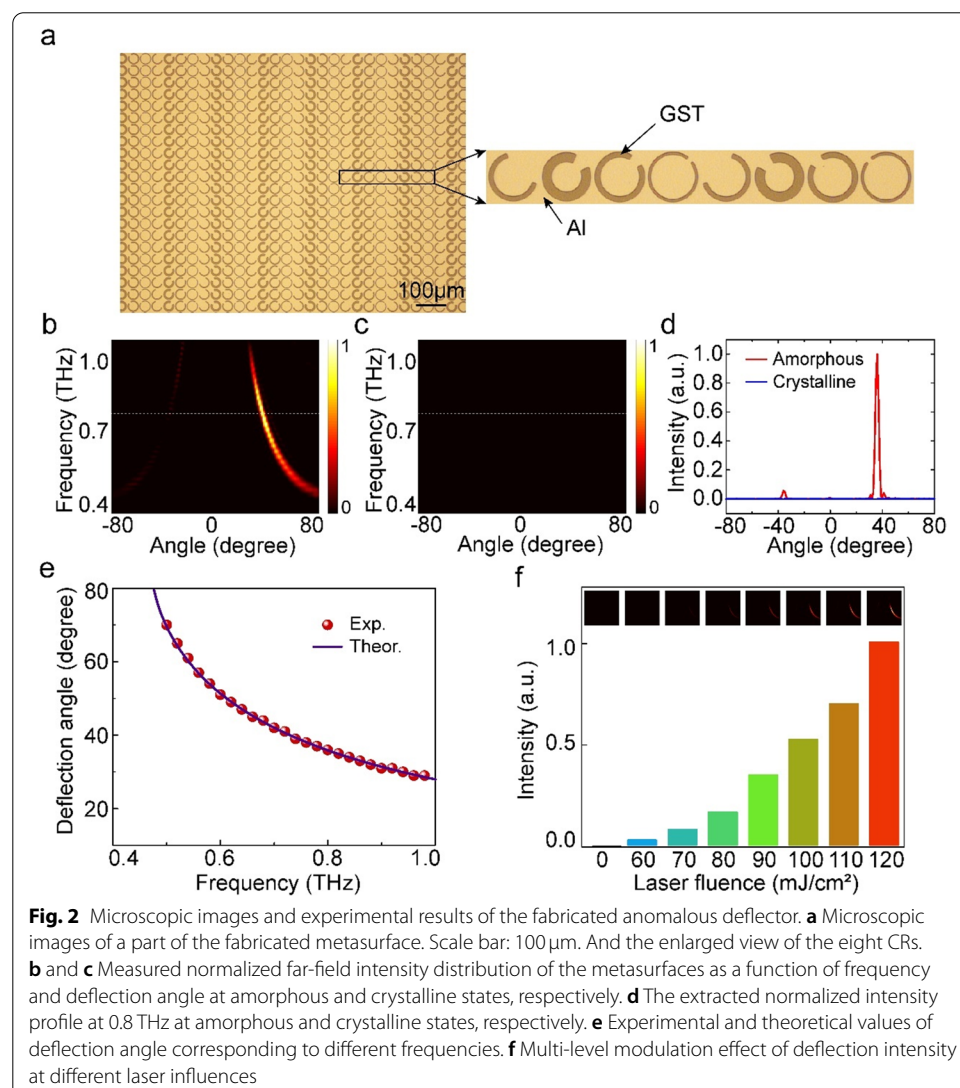
Results and discussion

To realize diverse active tuning devices using phase discontinuities metasurfaces, it is necessary to achieve a set of unit cells that enable phase shift covering the 2π range and nearly constant transmission amplitude in a wide frequency range. C-shaped split-ring resonators (CSRRs), which perform strong resonance responses to terahertz radiation, have been used to realize broadband wavefront manipulation [19, 20, 29, 35, 60], and their complementary configuration CRs have similar characteristics due to the Babinet principle [61]. Here, CRs are designed as basic unit cells whose symmetry lines are oriented either $+45°$ or $-45°$ with respect to the x-axis, as shown in Fig. 1a. Due to the symmetry, the incident y polarization will be partially converted

Fig. 1 Schematic of the basic functional units. **a** Schematic view of a single CR and corresponding geometric parameters. α is the opening angle, w is the width, r is the outer radius and $P = 80\,\mu m$ is the period. **b** Eight CRs unit cell. **c** and **d** simulated phase and amplitude spectra of cross-polarized components of each unit cell

into x-polarized components, whose phase and amplitude could be modulated by varying the opening angle α, line width w, and radius r. In addition, by mirroring the structure along the y-axis, a phase shift of π will be achieved while maintaining a constant amplitude. Numerical simulations are performed to choose the appropriate structures with computer simulation technology (CST) Microwave Studio. CRs made from aluminum (Al) are fabricated on a 2 mm-thick silicon substrate. Y-polarized plane waves are normally incident on a structure with varying geometrical parameters and scattered x-polarized radiations are detected. Here, an eight-level phase distribution is adopted, and four CRs are selected with a $\pi/4$ phase change interval and uniform transmission amplitude. The geometric parameters are as follows: (r, w, α) = (37 μm, 8 μm, 120°), (37 μm, 15 μm, 40°), (38 μm, 9 μm, 30°), and (38 μm, 5 μm, 12°) and the period size of a single unit $P = 80$ μm. By mirroring the structure, eight units are obtained covering the 2π phase shift from unit cells #1 to #8, as shown in Fig. 1b, which exhibit a broadband resonance response range from 0.4 THz to 0.8 THz, as shown in Fig. 1c and d. This characteristic allows the design of various functional devices that can modulate the wavefront of the cross-polarized components. Broadband, nonvolatile and reconfigurable THz modulation devices could be realized by combining 100 nm-thick GST deposited between silicon and Al. Here, several

THz modulators are proposed, and all the samples are fabricated by conventional lithography.

A cross-polarized anomalous deflector with a linear phase profile is first designed. Figure 2a shows microscopic images of the fabricated sample. A fiber-based angle-resolved terahertz time-domain spectroscopy (FAT-TDS) system [30] is applied to characterize the sample. The THz waves are transmitted and received by a pair of photoconductive antennas. The generated THz radiation is collimated by a lens and normally incident on the metasurfaces from the structure side, and a 45° polarizer and a y polarizer are placed before the sample so that the incident polarization is y polarization, which is perpendicular to the phase gradient. The scattered terahertz wave is focused on the detector by the second lens, and the detector and the second lens are installed on a rail of the rotating stage to collect deflected radiation at different angles. During the measurement, the stage is gradually rotated from $-80°$ to $80°$, and the scanning accuracy is 1°. The measured normalized intensity as a function of frequency and angle is shown in Fig. 2b

Fig. 2 Microscopic images and experimental results of the fabricated anomalous deflector. **a** Microscopic images of a part of the fabricated metasurface. Scale bar: 100 μm. And the enlarged view of the eight CRs. **b** and **c** Measured normalized far-field intensity distribution of the metasurfaces as a function of frequency and deflection angle at amorphous and crystalline states, respectively. **d** The extracted normalized intensity profile at 0.8 THz at amorphous and crystalline states, respectively. **e** Experimental and theoretical values of deflection angle corresponding to different frequencies. **f** Multi-level modulation effect of deflection intensity at different laser influences
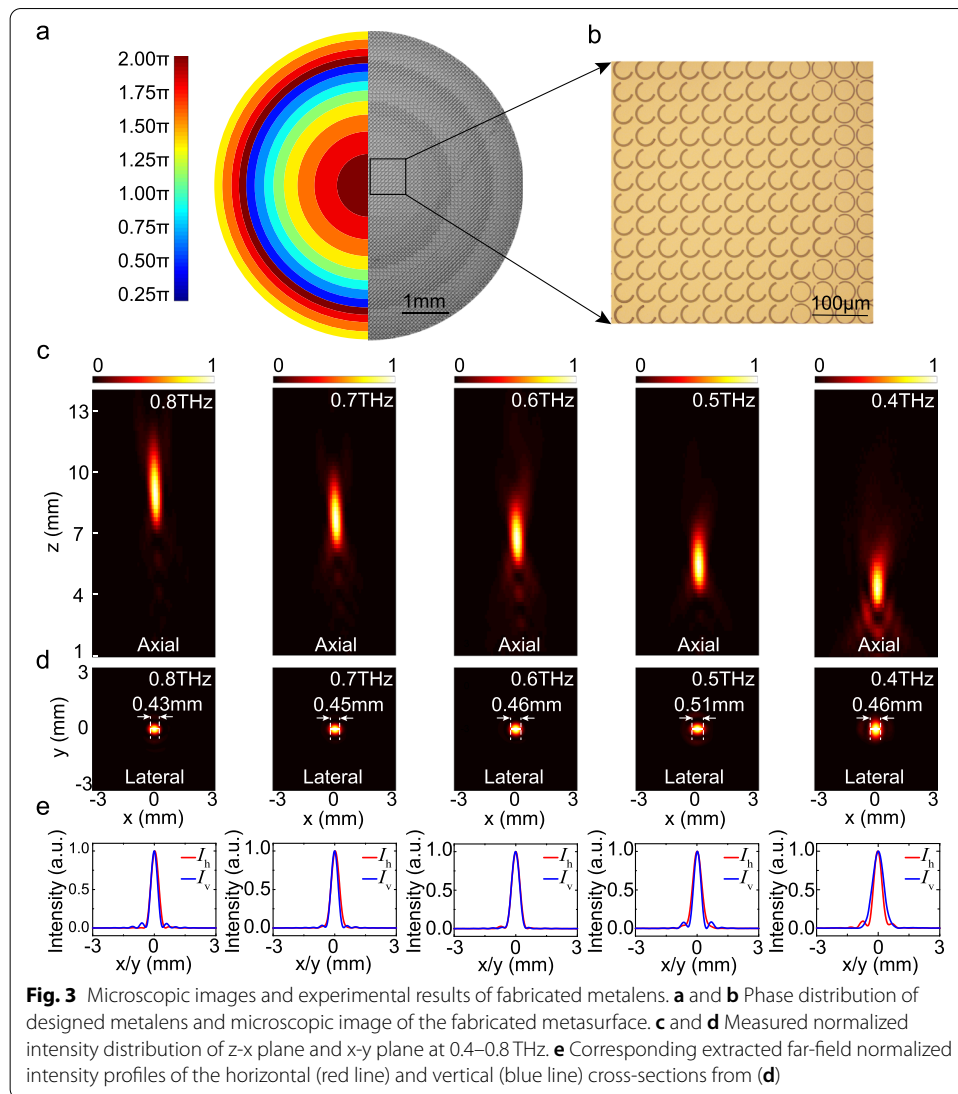
when GST is in the amorphous state. It can be seen from the results that the deflector exhibits broadband deflection characteristics from 0.5 THz to 1 THz. Nearly all of the energy is steered towards a certain angle under a fixed frequency. Then, we heated the sample at 300 °C for two minutes to transition GST from an amorphous state to a crystalline state, corresponding to low conductivity/high transmittance and high conductivity/low transmittance, respectively. The scanning results are shown in Fig. 2c. Most of the energy is reflected and absorbed; thus, the deflection effect is completely closed. Figure 2d shows the extracted normalized intensity profile at 0.8 THz corresponding to the two states. The deflection angle is 36° at the amorphous state, which is in good agreement with the result calculated by the generalized Snell's law, $\theta = \sin^{-1}[\lambda/(8P)] = 35.87°$, where λ is the wavelength and P is the unit period. In the crystalline state, the deflection intensity is almost zero across the entire scanning angular range. An acceptable cross-polarized deflection switching device is realized. In the "ON" state, nearly all the energy is deflected to the first diffraction order while it is reflected and absorbed in the "OFF" state. Figure 2e shows the deflection angle at the different frequencies by theoretical calculations and experimental measurements, which are in good agreement. In addition to the two states of "ON" and "OFF", we also demonstrate the effect of multilevel modulation by irradiation with ns laser pulses, as shown in Fig. 2f. By tuning the laser influence from 60 mJ/cm^2 to 120 mJ/cm^2 with a step of 10 mJ/cm^2, different deflection intensities are realized, which exhibit varying brightness in the inset of Fig. 2f. With increasing laser influence, the deflection intensity gradually increases while the frequency range and deflection angle remain constant. This effect comes from the increase in the amorphization degree of GST, which significantly increases the transmission. Thus, broadband, multilevel, nonvolatile, and reconfigurable THz deflectors are achieved.

Next, to demonstrate the versatile abilities of the proposed metasurface, a metalens is designed and experimentally characterized. The basic design strategy of a metasurface lens is shown in Fig. 3a. The phase distribution of the metasurface is designed to enable the radiation scattered by unit cells to constructively interfere at the focal plane, similar to the waves that emerge from the conventional lens. The hyperboloidal phase profile is designed according to

$$\phi(x,y) = -\frac{2\pi}{\lambda}\left(\sqrt{x^2 + y^2 + f^2} - f\right) \tag{1}$$

where λ is the wavelength and f is the designed focal length. Here, we set $f = 10$ mm at 0.8 THz. According to the calculated phase distribution, we arrange the suitable CRs according to position, as illustrated in Fig. 3a. Figures 3a and b show microscopic images fabricated by conventional photolithography, and the diameter of the lens is designed to be 5.12 mm with a numerical aperture (NA) of 0.26.

A near-field scanning terahertz microscopy (NSTM) system [32], which can realize three-dimensional scanning of the x-polarized electric field, is applied to characterize the performance of the metasurface lens in the target range from 0.4 to 0.8 THz. Figure 3c demonstrates the measured normalized intensity distribution at the z-x planes in 0.2 mm steps from 1 mm to 14 mm under y-polarized incidence when GST is in the amorphous state. It can be seen from the results that the lens exhibits a broadband focusing effect from 0.4 to 0.8 THz, and with decreasing frequency, the focal length gradually

Fig. 3 Microscopic images and experimental results of fabricated metalens. **a** and **b** Phase distribution of designed metalens and microscopic image of the fabricated metasurface. **c** and **d** Measured normalized intensity distribution of z-x plane and x-y plane at 0.4–0.8 THz. **e** Corresponding extracted far-field normalized intensity profiles of the horizontal (red line) and vertical (blue line) cross-sections from (**d**)

decreases from 8.8 mm to 4.2 mm. This reduction law can be inferred from Eq. (1). The difference between the experimentally measured and designed focal lengths is mainly due to the focused instead of parallel terahertz waves incident on the sample. To further characterize the broadband focal performance of the lens, the intensity distributions of the x-y focal plane at the corresponding frequency range are measured in 0.1 mm steps from −3 mm to 3 mm, as shown in Fig. 3d. The focal spots appear to have good round shapes in a broadband frequency range, and nearly all the energy is concentrated in the focal spots. The obtained horizontal full widths at half maximum (FWHM) at 0.8 THz is 0.43 mm. Figure 3e illustrates the intensity distribution of the horizontal (red line) and vertical (blue line) cross-sections in Fig. 3d. The reasons for the difference in FWHM of different frequencies are mainly due to the variation in wavelength λ, focal length f, and diameter of the incident terahertz beam L, which can be expressed as $D \propto \lambda f / L$.
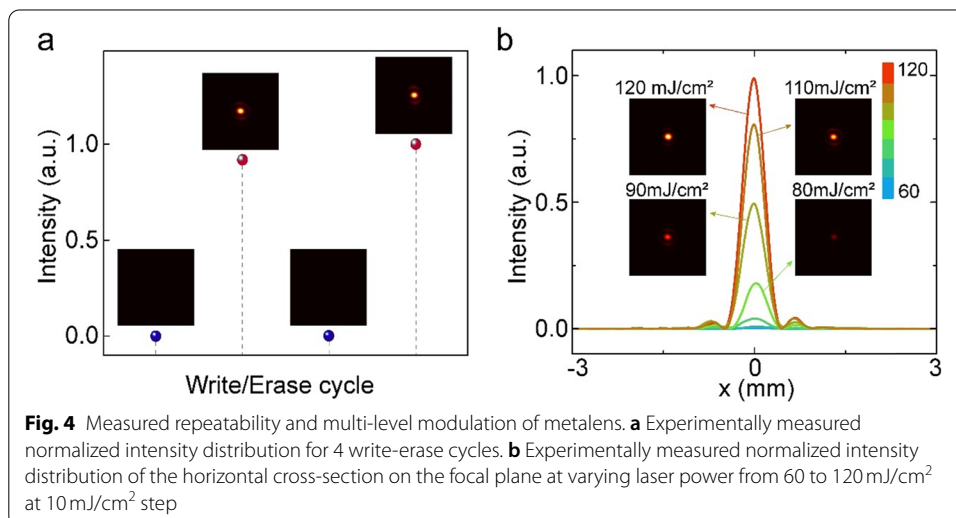
To illustrate the remarkable characteristics of the designed device, the repeatability of the reversible transition between amorphous and crystalline states is measured

experimentally. Figure 4a shows the normalized peak focusing intensity for 4 write-erase cycles, and the corresponding focal plane intensity distributions are shown in the illustration. Here, we heat the entire sample on a hot plate to induce crystallization, and the focal effect is measured after baking the sample at 300 °C for 2 min. As we can see from the results, the focal spot has completely disappeared, the peak intensity is close to zero, and the device works in the "OFF" state. Then, a single 7-ns laser pulse with 120 mJ/cm^2 is applied to reamorphize the GST, the device is turned on again, which performs as an excellent lens, and another write-erase cycle is carried out, which demonstrates the repeatability of the modulator. The slight increase of intensity is due to the instability of laser fluence and measurement system. In addition to binary modulation, by tuning the laser influence from 60 to 120 mJ/cm^2 at a 10 mJ/cm^2 step, we experimentally measure the multilevel modulation of the focused intensity by partially or completely reamorphizing the crystalline GST. Figure 4b shows the normalized intensity distribution of the horizontal cross-section at the focal plane. When the laser fluence is smaller than 120 mJ/cm^2, the GST are at intermediate states composed of amorphous and crystalline states. As the laser fluence increases from 60 to 120 mJ/cm^2, the proportions of amorphous GST gradually increase, so does the THz transmission and the intensity at the focal spot, as shown in the inset of Fig. 4b.

Finally, a focusing optical vortex (FOV) generator is further proposed. It is necessary to combine two distinct functionalities of focusing and spiral phase plates into one metasurface to generate FOVs, whose phase distribution profiles can be expressed as follows:
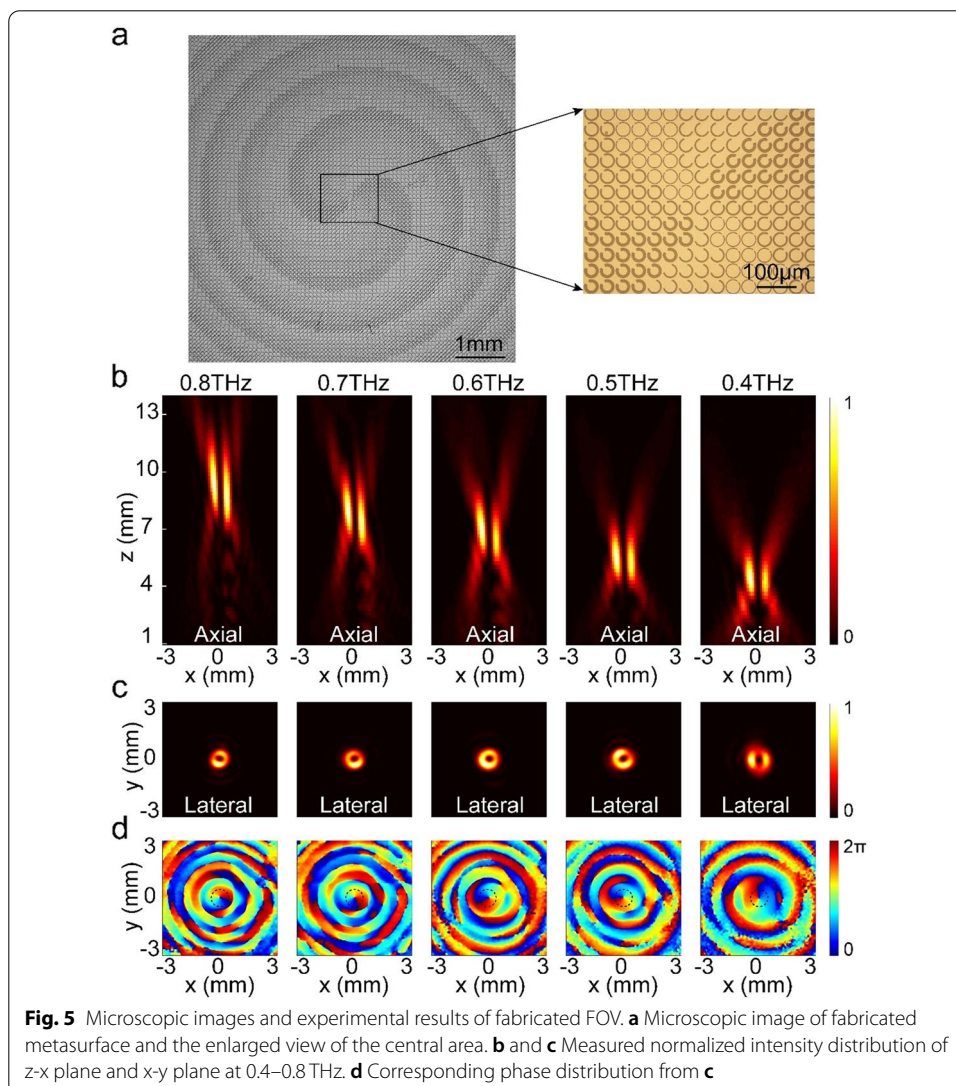
$$\phi(\rho, \theta) = -\frac{2\pi}{\lambda} \left(\sqrt{\rho^2 + f^2} - f \right) + l \times \theta \tag{2}$$

where (ρ, θ) is the polar coordinate of any point on the metasurface, λ is the design wavelength, f is the focal length and l is the topological charge. Then, we can obtain the spatial distribution of the phase profile, and the corresponding phase distribution is realized by eight-order phase discretized CRs. First, the FOV generator with topological charges

Fig. 4 Measured repeatability and multi-level modulation of metalens. **a** Experimentally measured normalized intensity distribution for 4 write-erase cycles. **b** Experimentally measured normalized intensity distribution of the horizontal cross-section on the focal plane at varying laser power from 60 to 120 mJ/cm^2 at 10 mJ/cm^2 step

of $l = +1$ and focal length $f = 10$ mm at 0.8 THz is demonstrated. Part of the fabricated metasurface and an enlarged view of the central area are shown in Fig. 5a.

The above mentioned NSTM system is used to experimentally characterize the FOV, a y-polarized terahertz beam is incident on the metasurface, and x-polarized radiation is received. The normalized intensity distribution of the z-x cross-section is measured in 0.2 mm steps from 1 mm to 14 mm in the z-direction and 0.1 mm steps in the x-direction from −3 mm to 3 mm, as shown in Fig. 5b. It can be seen from the results that the intensity distributions exhibited hollow focused characteristics with different focal lengths from 0.4 THz to 0.8 THz, which is a representative behavior of FOVs and is the same as the principle of focusing metalenses, the focal lengths are distinct at different frequencies. To further demonstrate the characteristics of the FOV, the x-y plane intensities and phase distributions are measured at corresponding focal planes in 0.1 mm steps in the x-direction and y-direction from −3 mm to 3 mm, as shown in Fig. 5c and d. Good doughnut shape intensity distributions with a hollow center can be seen, which is a

Fig. 5 Microscopic images and experimental results of fabricated FOV. **a** Microscopic image of fabricated metasurface and the enlarged view of the central area. **b** and **c** Measured normalized intensity distribution of z-x plane and x-y plane at 0.4–0.8 THz. **d** Corresponding phase distribution from **c**
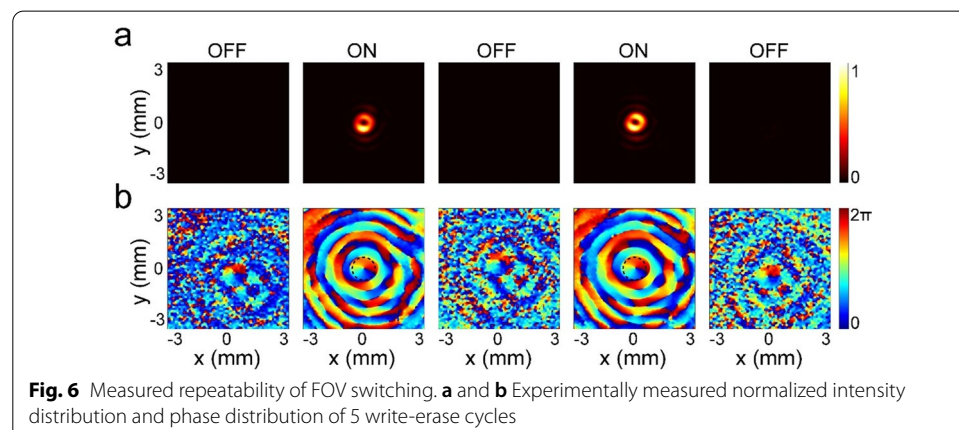
direct consequence of the self-canceling effect. Due to the focusing effect, nearly all the energy converges into the annulus. Figure 5d shows that there is a spiral phase distribution in the central area (black dotted line) with the phase singularity in the center, and the phase has undergone a 2π shift around the closed-loop, which is the clear feature of the +1st-order vortex beam.

To evaluate the repeatability of the designed FOV, write-erase cyclability is performed. As shown in Figs. 6a and b, normalized intensity distributions and phase distributions at 0.8 THz are characterized. First, the metasurface is heated on a hot plate at 300 °C for 2 min to fully transition GST from an amorphous to a crystalline state, which erases all the information and turns off the FOV. The intensity distribution appears as a uniform zero value with an irregular phase distribution. By applying a 7-ns single laser pulse with 120 mJ/cm^2, the GST is reamorphized, and the FOV is turned on again with a constant focal length, intensity, and phase distributions. Five switching cycles are carried out, which demonstrate that the FOV can be written and erased repeatedly and that more cycles can be performed. In addition to the 1st-order FOV device, higher-order FOV devices could be realized. In the supplementary information, we show the designed and experimentally measured -2nd-order FOV device.

Conclusion

We demonstrate nonvolatile, reconfigurable, multilevel and broadband terahertz modulators that exploit large conductivity changes induced by phase changes in GSTs and phase-discontinuities metasurface. By varying the geometric parameters of CRs, eight-level phase distributions are realized. Then, the anomalous deflector, metalens and focusing optical vortex generator are designed, fabricated and experimentally measured. By gradually tuning the fluence of laser pulses, multilevel intensity modulation is realized. The states of GST can be repeatedly switched between amorphous, crystalline states, and intermediate states on a large scale with the help of nanosecond laser pulses and thermal annealing. Specifically, we believe that this is the novel attempt to combine phase change materials with wavefront modulation metasurfaces to achieve terahertz modulators that are nonvolatile without constant energy to maintain, reconfigurable, multilevel, including many intermediate states, and broadband from 0.4 to 0.8 THz. We expect that the proposed novel THz modulators will be helpful for THz

Fig. 6 Measured repeatability of FOV switching. **a** and **b** Experimentally measured normalized intensity distribution and phase distribution of 5 write-erase cycles

imaging, sensing, and high-speed communication. Furthermore, the proposed metasurfaces are easy to fabricate and compatible with semiconductor technologies, making them very promising in developing next-generation ultracompact and multifunctional THz devices.

Methods

Sample fabrication

Two-millimeter-thick high-resistivity silicon (Si) wafers were taken as the substrates and cleaned ultrasonically in acetone, isopropanol, and deionized water in sequence before deposition. Then, the 100-nm-thick GST film was direct current magnetron sputter-deposited on the Si substrate. Al (200-nm-thick) was deposited on the GST film, and the CRs were fabricated by conventional lithography procedures.

Experimental characterization

A fiber-based angle-resolved terahertz time-domain spectroscopy (FAT-TDS) system (Supporting information, Fig. S3 a) is used to characterize the dynamic beam splitter. The generated THz waves are first collimated by a lens L1, which is then normally illuminated on the sample. Then, the scattered terahertz waves are collected on the receiver by a second lens L2. The sample is fixed at the center of a rotation stage. To realize cross-polarization characterization, three metallic grid-based terahertz linear polarizers P1, P2 and P3 are applied. Two of them (P1 and P2) are placed before the sample, which are used to allow 45°-polarized and y-polarized transmission in sequence. The third (P3) is after the sample to allow x-polarized transmission. The receiver, the second lens L2, and the third polarizer P3 are fixed on a rail mounted on the motorized rotator to collect the output THz radiation.

A near-field scanning terahertz microscopy (NSTM) system (Supporting information, Fig. S3 b) is used to characterize the metalens and FOV generator. Femtosecond laser pulses with 1550 nm central wavelength and 50 fs pulse width are split into two beams to generate and detect the terahertz waves. A homemade photoconductive antenna is used to generate THz waves, and a commercially available THz near-field probe is used for detection. The probe is mounted on a 2D translation stage in the x-y plane, and the sample is on a 1D translation stage in the z-axis direction. 3D electric field scanning can be realized. The generated THz waves are collimated by a lens L1 and then detected by the probe. The metasurface is placed between the lens and the probe. Similar to the FAT-TDS system, two polarizers P1 and P2 are used to allow only the y-polarized THz waves to illuminate the sample. The 3D electric field of devices is detected at 0.1 mm step in the x-direction and y-direction from -3 mm to $+3$ mm and 0.2 mm step in the z-direction from 1 mm to 14 mm.

Abbreviations
PCM: Phase change material; THz: Terahertz; GST: $Ge_2Sb_2Te_5$; FOV: Focusing optical vortex; LCs: Liquid crystals; MEMS: Micro electromechanical systems; CRs: C-shaped slit resonators; FAT-TDS: Fiber-based angle-resolved terahertz time-domain spectroscopy; NSTM: Near-field scanning terahertz microscopy; CSRRs: C-shaped split-ring resonators; CST: Computer simulation technology; Si: Silicon; Al: Aluminum; NA: Numerical aperture; FWHM: Full widths at half maximum; 1D: One-dimensional; 3D: Three-dimensional.

Supplementary Information

The online version contains supplementary material available at https://doi.org/10.1186/s43074-022-00053-5.

Availability of data and materials
The data and the relevant methods are available on request from the corresponding authors.

Declarations

Ethics approval and consent to participate
There is no ethics issue for this paper.

Consent for publication
All authors agreed to publish this paper.

Competing interests
There are no competing interests for this paper.

Author details
[1]Center for Terahertz Waves and School of Precision Instrument and Optoelectronics Engineering, Key Laboratory of Optoelectronic Information Technology (Ministry of Education of China), Tianjin University, Tianjin 300072, China. [2]School of Optoelectronic Engineering and Instrumentation Science, Dalian University of Technology, Dalian 116024, People's Republic of China. [3]Georgia Tech Shenzhen Institute (GTSI), Tianjin University, Shenzhen 518067, China.

References

1. Siegel PH. Terahertz technology. IEEE Trans Microw Theory Tech. 2002;50(3):910–28.
2. Dragoman D, Dragoman M. Terahertz fields and applications. Prog Quantum Electron. 2004;28(1):1–66.
3. Tonouchi M. Cutting-edge terahertz technology. Nat Photonics. 2007;1(2):97–105.
4. Pickwell E, Wallace VP. Biomedical applications of terahertz technology. J Phys D Appl Phys. 2006;39(17):R301.
5. Fan S, He Y, Ung BS, et al. The growth of biomedical terahertz research. J Phys D Appl Phys. 2014;47(37):374009.
6. Beard MC, Turner GM, Schmuttenmaer CA. Terahertz spectroscopy. J Phys Chem B. 2002;106(29):7146–59.
7. Jepsen PU, Cooke DG, Koch M. Terahertz spectroscopy and imaging–modern techniques and applications. Laser Photon Rev. 2011;5(1):124–66.
8. Debus C, Bolivar PH. Frequency selective surfaces for high sensitivity terahertz sensing. Appl Phys Lett. 2007;91(18):184102.
9. Beruete M, Jáuregui-López I. Terahertz sensing based on metasurfaces. Adv Opt Mater. 2020;8(3):1900721.
10. Mittleman DM. Twenty years of terahertz imaging. Opt Express. 2018;26(8):9417–31.
11. Tzydynzhapov G, Gusikhin P, Muravev V, et al. New real-time sub-terahertz security body scanner. J Infrared Millim Terahertz Waves. 2020;41(6):632–41.
12. Nagatsuma T, Ducournau G, Renaud CC. Advances in terahertz communications accelerated by photonics. Nat Photonics. 2016;10(6):371–9.
13. Yang Y, Yamagami Y, Yu X, et al. Terahertz topological photonics for on-chip communication. Nat Photonics. 2020;14(7):446–51.
14. Sengupta K, Nagatsuma T, Mittleman DM. Terahertz integrated electronic and hybrid electronic–photonic systems. Nat Electron. 2018;1(12):622–35.
15. Degl'Innocenti R, Kindness SJ, Beere HE, et al. All-integrated terahertz modulators. Nanophotonics. 2018;7(1):127–44.
16. Cong L, Han J, Zhang W, et al. Temporal loss boundary engineered photonic cavity. Nat Commun. 2021;12(1):1–8.
17. Yu N, Genevet P, Kats MA, et al. Light propagation with phase discontinuities: generalized laws of reflection and refraction. Science. 2011;334(6054):333–7.

18. Huang L, Chen X, Muhlenbernd H, et al. Dispersionless phase discontinuities for controlling light propagation. Nano Lett. 2012;12(11):5750–5.
19. Zhang X, Tian Z, Yue W, et al. Broadband terahertz wave deflection based on C-shape complex metamaterials with phase discontinuities. Adv Mater. 2013;25(33):4567–72.
20. Liu L, Zhang X, Kenney M, et al. Broadband metasurfaces with simultaneous control of phase and amplitude. Adv Mater. 2014;26(29):5031–6.
21. Papakostas A, Potts A, Bagnall DM, et al. Optical manifestations of planar chirality. Phys Rev Lett. 2003;90(10):107404.
22. Grady NK, Heyes JE, Chowdhury DR, et al. Terahertz metamaterials for linear polarization conversion and anomalous refraction. Science. 2013;340(6138):1304–7.
23. Wang Q, Plum E, Yang Q, et al. Reflective chiral meta-holography: multiplexing holograms for circularly polarized waves. Light Sci Appl. 2018;7(1):1–9.
24. Ye W, Zeuner F, Li X, et al. Spin and wavelength multiplexed nonlinear metasurface holography. Nat Commun. 2016;7(1):1–7.
25. Huang L, Zhang S, Zentgraf T. Metasurface holography: from fundamentals to applications. Nanophotonics. 2018;7(6):1169–90.
26. Ma Q, et al. Smart metasurface with self-adaptively reprogrammable functions. Light Sci Appl. 2019;8(1):98.
27. Ma Q, Cui TJ. Information metamaterials: bridging the physical world and digital world. PhotoniX. 2020;1(1):1–32.
28. Chen X, Huang L, Mühlenbernd H, et al. Dual-polarity plasmonic metalens for visible light. Nat Commun. 2012;3(1):1–6.
29. Wang Q, Zhang X, Xu Y, et al. A broadband metasurface-based terahertz flat-lens array. Adv Opt Mater. 2015;3(6):779–85.
30. Xu Y, Li Q, Zhang X, et al. Spin-decoupled multifunctional metasurface for asymmetric polarization generation. ACS Photonics. 2019;6(11):2933–41.
31. Cong L, Srivastava YK, Zhang H, et al. All-optical active THz metasurfaces for ultrafast polarization switching and dynamic beam splitting. Light Sci Appl. 2018;7:28.
32. Xu Y, Zhang H, Li Q, et al. Generation of terahertz vector beams using dielectric metasurfaces via spin-decoupled phase control. Nanophotonics. 2020;9(10):3393–402.
33. Ni X, Kildishev AV, Shalaev VM. Metasurface holograms for visible light. Nat Commun. 2013;4(1):1–6.
34. Zhang X, Xu Y, Yue W, et al. Anomalous surface wave launching by handedness phase control. Adv Mater. 2015;27(44):7123–9.
35. Xu Q, Zhang X, Wei M, et al. Efficient metacoupler for complex surface plasmon launching. Adv Opt Mater. 2018;6(5):1701117.
36. Wang L, Lin XW, Hu W, et al. Broadband tunable liquid crystal terahertz waveplates driven with porous graphene electrodes. Light Sci Appl. 2015;4(2):e253.
37. Shrekenhamer D, Chen WC, Padilla WJ. Liquid crystal tunable metamaterial absorber. Phys Rev Lett. 2013;110(17):177403.
38. Chen HT, Padilla WJ, Zide JMO, et al. Active terahertz metamaterial devices. Nature. 2006;444(7119):597–600.
39. Zhou J, Chowdhury DR, Zhao R, et al. Terahertz chiral metamaterials with giant and dynamically tunable optical activity. Phys Rev B. 2012;86(3):035448.
40. Pitchappa P, Manjappa M, Ho CP, et al. Active control of electromagnetically induced transparency analog in terahertz MEMS metamaterial. Adv Opt Mater. 2016;4(4):541–7.
41. Cong L, Pitchappa P, Lee C, et al. Active phase transition via loss engineering in a terahertz MEMS metamaterial. Adv Mater. 2017;29(26):1700733.
42. Manjappa M, Pitchappa P, Wang N, et al. Active control of resonant cloaking in a terahertz MEMS metamaterial. Adv Opt Mater. 2018;6(16):1800141.
43. Cong L, Pitchappa P, Wu Y, et al. Active multifunctional microelectromechanical system metadevices: applications in polarization control, wavefront deflection, and holograms. Adv Opt Mater. 2017;5(2):1600716.
44. Lee SH, Choi M, Kim TT, et al. Switching terahertz waves with gate-controlled active graphene metamaterials. Nature Mater. 2012;11(11):936–41.
45. Li Q, Tian Z, Zhang X, et al. Active graphene–silicon hybrid diode for terahertz waves. Nat Commun. 2015;6(1):1–6.
46. Liu M, Plum E, Li H, et al. Switchable chiral mirrors. Adv. Opt Mater. 2020;8:15.
47. Pitchappa P, Kumar A, Prakash S, et al. Chalcogenide phase change material for active terahertz photonics. Adv Mater. 2019;31(12):1808157.
48. Makino K, Kato K, Saito Y, et al. Terahertz spectroscopic characterization of Ge2Sb2Te5 phase change materials for photonics applications. J Mater Chem C Mater. 2019;7(27):8209–15.
49. Pitchappa P, Kumar A, Prakash S, et al. Volatile ultrafast switching at multilevel nonvolatile states of phase change material for active flexible terahertz metadevices. Adv Funct Mater. 2021;31(17):2100200.
50. Cong L, Singh R. Spatiotemporal dielectric metasurfaces for unidirectional propagation and reconfigurable steering of terahertz beams. Adv Mater. 2020;32(28):2001418.
51. Dong W, Qiu Y, Zhou X, et al. Tunable mid-infrared phase-change metasurface. Adv Opt Mater. 2018;6(14):1701346.
52. Cao T, Zhang X, Dong W, et al. Tuneable thermal emission using chalcogenide metasurface. Adv Opt Mater. 2018;6(16):1800169.
53. Ríos C, Stegmaier M, Hosseini P, et al. Integrated all-photonic non-volatile multi-level memory. Nat Photonics. 2015;9(11):725–32.
54. Farmakidis N, Youngblood N, Li X, et al. Plasmonic nanogap enhanced phase-change devices with dual electrical-optical functionality. Sci Adv. 2019;5(11):eaaw2687.
55. Tuma T, Pantazi A, Le Gallo M, et al. Stochastic phase-change neurons. Nat Nanotechnol. 2016;11(8):693–9.
56. Feldmann J, Stegmaier M, Gruhler N, et al. Calculating with light using a chip-scale all-optical abacus. Nat Commun. 2017;8(1):1–8.
57. Hosseini P, Wright CD, Bhaskaran H. An optoelectronic framework enabled by low-dimensional phase-change films. Nature. 2014;511(7508):206–11.

58. de Galarreta CR, Sinev I, Alexeev AM, et al. Reconfigurable multilevel control of hybrid all-dielectric phase-change metasurfaces. Optica. 2020;7(5):476–84.
59. Lin QW, Wong H, Huitema L, et al. Coding Metasurfaces with reconfiguration capabilities based on optical activation of phase-change materials for terahertz beam manipulations. Adv Opt Mater. 2021;10(1):2101699.
60. Su X, Ouyang C, Xu N, et al. Active metasurface terahertz deflector with phase discontinuities. Opt Express. 2015;23(21):27152–8.
61. Bitzer A, Ortner A, Merbold H, et al. Terahertz near-field microscopy of complementary planar metamaterials: Babinet's principle. Opt Express. 2011;19(3):2537–45.

Publisher's Note

Springer Nature remains neutral with regard to jurisdictional claims in published maps and institutional affiliations.